Natural iron fertilization moderates hydrothermal mercury inputs from arc volcanoes

Natalia Torres-Rodriguez, Jingjing Yuan, Aurélie Dufour, Igor Živković, David Point, Cédric Boulart, Joël Knoery, Milena Horvat, David Amouroux, Sophie Bonnet, et al.

Natural iron fertilization moderates hydrothermal mercury inputs from arc volcanoes

Natalia Torres-Rodriguez[1*], Jingjing Yuan[2°], Aurélie Dufour[1], Igor Živković[3], David Point[4], Cédric Boulart[5], Joël Knoery[6], Milena Horvat[3], David Amouroux[7], Sophie Bonnet[1], Cécile Guieu[8], Ruoyu Sun[2], Lars-Eric Heimbürger-Boavida[1*]

1. Aix Marseille Université, CNRS/INSU, Université de Toulon, IRD, Mediterranean Institute of Oceanography (MIO), Marseille, 13009, France
2. Institute of Surface-Earth System Science, School of Earth System Science, Tianjin University, 300072 Tianjin, China.
3. Jozef Stefan Institute, Department of Environmental Sciences, Ljubljana, 1000, Slovenia
4. Géosciences Environnement Toulouse GET CNRS UMR 5563, IRD/UPS/CNES, Université de Toulouse, Toulouse, 31400, France
5. University of Brest, CNRS, IRD, Ifremer, LEMAR, IUEM, Plouzané, 29280, France
6. Ifremer, CCEM Contamination Chimique des Ecosystèmes Marins, Nantes, 44311, France
7. Université de Pau et des Pays de l'Adour, E2S UPPA, CNRS, IPREM, Institut des Sciences Analytiques et de Physico-chimie pour l'Environnement et les Matériaux, Pau, 64000, France
8. Laboratoire d'Océanographie de Villefranche (LOV), Institut de la Mer de Villefranche, CNRS, Sorbonne Université, Villefranche-sur-Mer, 06230, France.

*Corresponding authors: natalia.torres-rodriguez@mio.osupytheas.fr, lars-eric.heimburger@mio.osupytheas.fr.

Abstract

Methylmercury is a bioaccumulative neurotoxin that poses severe risks to marine ecosystems and human health worldwide. Hydrothermal systems and submarine volcanoes are natural sources of mercury, yet the magnitude of emissions, their transport, and their impact on marine ecosystems remain poorly understood. Quantifying natural mercury fluxes is essential to understanding anthropogenic perturbations and guiding effective reduction strategies. We investigate hydrothermal mercury inputs at the Tonga volcanic arc and their impact on the local ecosystem. Our results show that hydrothermal and volcanic activity in the Tonga Arc increases mercury concentrations in seawater. Comprehensive surveys identified mercury-rich plumes (up to 22.7 pmol l^{-1}) associated with high mercury fluxes (4,763 pmol m^{-2} day^{-1}) reaching productive surface waters, resulting in an estimated total flux of 4.23 t y^{-1} for the entire Tonga Arc. Despite these significant inputs, mercury concentrations in phytoplankton remain unexpectedly low. We demonstrate that phytoplankton blooms, stimulated by natural iron fertilization from hydrothermal sources, dilute mercury at the cellular level, reducing the impact of hydrothermal mercury. Additionally, we provide a revised global estimate of hydrothermal mercury inputs with a maximum of 120 t y^{-1}, which is considerably lower than atmospheric and riverine inputs to the ocean.

Keywords

Hydrothermal vents, Submarine volcanoes, Phytoplankton, Minamata Convention on Mercury

Synopsis

Our study reveals that arc volcanoes release significant amounts of mercury. The simultaneous release of iron drives abundant phytoplankton blooms, which, in turn, dilute mercury concentrations at the cellular level.

TOC

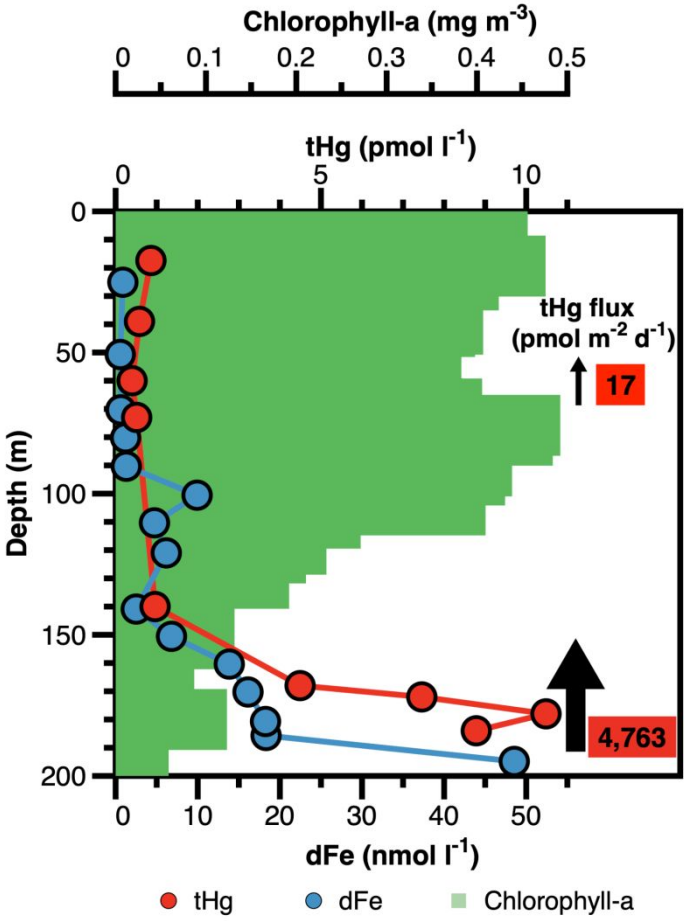

Introduction

Mercury (Hg) is a global contaminant threatening the environment and human health primarily through its accumulation in seafood [1,2]. The Minamata Convention on Mercury aims to protect human and ecosystem health from Hg pollution. Quantifying natural Hg fluxes is crucial to understand how anthropogenic Hg emissions have altered the global Hg cycle and effectively guide reduction measures. While global anthropogenic Hg inputs are well-quantified to 2,600–3,600 t y^{-1} [3,4], significant uncertainties persist regarding natural inputs. The ocean receives natural and anthropogenic Hg from atmospheric deposition, riverine inputs, and submarine groundwater discharge [5–7]. Submarine hydrothermal vents feed the ocean exclusively with natural Hg [8]. Measurements of Hg at the Trans-Atlantic Geotraverse hydrothermal vent site have been used to constrain the global hydrothermal Hg flux from mid-ocean ridges to 1.5 - 64.7 t y^{-1} [9]. However, this proposed hydrothermal Hg flux estimate is incomplete because it lacks inputs from other submarine geological settings such as arc systems, hot spots, and back-arc spreading centers.

Arc systems, often located at depths of less than 1,600 m [10], can directly deliver Hg-rich hydrothermal fluids to the surface waters, where Hg can enter and propagate through the marine food web. Some microorganisms process inorganic Hg into the bioaccumulative neurotoxin monomethylmercury (MMHg) [11]. MMHg bioconcentrates more than 100,000 times from seawater to phytoplankton to be further biomagnified and bioaccumulated in biota [12,13]. Studies on the impact of hydrothermal Hg on marine ecosystems consistently portray hydrothermal systems as significant sources of Hg to the marine food web, with phytoplankton inhabiting hydrothermal sites reportedly exhibiting elevated Hg concentrations [14–16]. Similarly, biota inhabiting deep hydrothermal vents exhibit elevated Hg levels [17–19], with isotopic signatures confirming hydrothermally-sourced Hg [20]. However, many of these studies focus primarily on specific ecosystem components, such as phytoplankton or fish, without considering Hg concentrations in hydrothermal fluids, plumes, surrounding seawater,

sediments, or the interplay between Hg and other trace elements released by the vents. This limited focus provides an incomplete assessment of the broader biogeochemical dynamics in hydrothermal systems. Here, we present Hg speciation data from a west-to-east cruise transect across the Lau Basin and Tonga Arc in the southwest Pacific Ocean. Using Hg speciation and isotope measurements from hydrothermal plume waters, seawater, phytoplankton, sinking particles, and sediments, alongside a review of Pacific Ocean Hg data, we assess the fate of the hydrothermal Hg inputs regionally and revise the overall global hydrothermal Hg flux.

Materials and Methods

We collected seawater, phytoplankton, sinking particles, and sediments during the GEOTRACES GPpr14 TONGA expedition onboard the RV L'Atalante in 2019. The cruise started in Nouméa in New Caledonia and extended until the South Pacific Gyre waters along the parallel 20°S, crossing the Lau Basin and the Tonga Arc (**Figure 1**). The cruise transect crossed four areas: Melanesian waters, Lau Basin, Tonga Arc, and South Pacific Gyre waters (**Figure 1. a**). The Melanesian waters, situated at the westernmost part of the transect, are characterized by numerous islands of the Melanesian archipelago, which serve as potential sources of trace metals and nutrients to the surrounding waters [21]. The central portion of the transect includes the hydrothermally influenced regions of the Lau Basin and the Tonga Arc. Hydrothermal plumes in the Lau Basin typically originate from deep sources greater than 1,000 m depth [22–24]. In contrast, the hydrothermal sources in the Tonga Arc are generally shallower [24]. To the east of the transect lies the South Pacific Gyre, a region characterized by open ocean waters depleted in iron (Fe) [25] and unaffected by hydrothermal plumes. Unfiltered seawater samples were collected along the cruise transect. We measured total Hg (tHg), defined as the sum of all Hg species, total dissolved gaseous Hg (DGM), which includes elemental gaseous Hg (Hg^0) and dimethylmercury (DMHg), and total methylated Hg (MeHg), defined as the sum of MMHg and DMHg. Divalent inorganic Hg (Hg^{2+}), DMHg, and Hg^0 were

calculated by mass balance in samples where all the other species were measured [26] (**Text S1**).

Eleven main stations were carried out during the cruise, referred to as 1-2-3 in the Melanesian Waters, 4,11,12 in the Lau Basin, 5,10 at the Tonga Arc, and 6,7,8 in the South Pacific Gyre waters. Seawater was collected at all stations using GOFLO bottles mounted on a trace metal-clean rosette (General Oceanics Inc., Model 1,018 Intelligent Rosette). The trace metal-clean rosette was attached to a 6 mm Kevlar line. The samples were collected under the ultra-clean conditions established by the GEOTRACES cookbook [27]. Phytoplankton was collected in the 11 main stations using phytoplankton nets (0-200 m, 200 µm). Samples from the phytoplankton nets were pre-concentrated onboard with a 100 µm sieve and preserved with 4% formaldehyde solution until Hg analysis in the laboratory. Sinking particles were collected onto two sediment traps deployed over a year at station 12 at 200 and 1000 m depth. Sediment cores were collected using an MC-8/100 multi-corer (Oktopus GmbH, Kiel, Germany) at stations 5, 10, and 12. Two hydrothermal shallow sources referred to as Panamax and Simone volcanoes, were identified from acoustic anomalies using a hull-mounted multibeam echosounder (EM - 710) operating at a 70 - 100 kHz frequency. The exploration of the hydrothermal and volcanic plumes was carried out with two turbidimeters (Seapoint Turbidity Meters), a pH sensor, and an Eh sensor (AMT GmBH) interfaced to an SBE911+ (Seabird Electronics) [28]. Seawater was collected in nine substations at the two volcanoes to study the hydrothermal impact in the water column. Samples for CH_4 were measured onboard immediately after collection using the headspace extraction technique followed by GC-FID. Seawater for dMn and dFe was filtered online through 0.45 µm with Supor® filters and acidified within 24 h collection. Concentrations of dFe were determined by flow injection analysis with chemiluminescence, while dMn was measured using a SeaFAST (ESI) system coupled to a high-resolution magnetic sector field inductively coupled mass spectrometer (SF-ICP-MS, Element XR) [28].

Preparation of the sampling material

We used perfluoroalkoxy alkane (PFA), Fluorinated ethylene propylene (FEP), and polyethylene terephthalate (PET) bottles for seawater collection. The PFA and FEP bottles underwent a two-step HCl cleaning process. In the first step, the bottle was rinsed with ultrapure water (18 MΩ cm, MQ), and bidistilled concentrated HCl was added to 10% of the bottle volume. The bottle was heated for 24 hours at 120 °C, cooled, rinsed three times with MQ water, and then subjected to a second cleaning step with reduced HCl concentration (10% v/v). After completing the two steps, bottles were stored with 0.4% v/v HCl at 10% of the volume until sampling. The PET bottles were used brand-new without cleaning.

Onboard mercury measurements

We measured tHg and DGM onboard (**Text S1**). The tHg samples were collected onto 70 ml FEP bottles and analyzed within two hours. Oxidizing bromine monochloride (BrCl, 0.2 M) and reducing stannous chloride ($SnCl_2$) solutions were prepared for the analysis. For the BrCl, the potassium bromide (KBr) and potassium bromate $KBrO_3$ powders (Sigma Aldrich) were heated for four hours at 250 °C to ensure cleanliness. The BrCl was prepared with bidistilled HCl and Hg-free powders. The $SnCl_2$ was purged with argon overnight to ensure the release of Hg traces. The BrCl solution was added to the samples in excess, equivalent to 0.1% of the volume of the sample, or until a transition of the sample to yellow was observed. The samples were left to react for at least 20 minutes. After this time, 35 ml of the sample was added to an impinger, together with $SnCl_2$, and the tHg concentration was measured by cold vapor atomic fluorescence (CV-AFS) [29]. The DGM samples were collected into 155 ml PET bottles and analyzed by CV-AFS without the addition of any reagent. After DGM analysis, the sample was acidified to 0.4% v/v HCl and stored until the MMHg analyses were done in the laboratory. The tHg and DGM measurements were calibrated with a 7-point calibration curve (R^2 > 0.9998) constructed with the reference material NIST-3133. Possible machine drift was

monitored by standard bracketing with NIST-3133 every six tHg and twelve DGM samples. Quality control was done with the certified reference materials ORMS-5 (National Research Council Canada) and ERM-CA400 (European reference materials). The measured tHg concentrations were 133 ± 4.2 pmol l^{-1} (n = 44) for ORMS-5 and 84.6 ± 3.7 pmol l^{-1} (n = 46) for ERM-CA400, well within the certified ranges (131 ± 6.5 pmol l^{-1} for ORMS-5 and 83.8 ± 5.5 pmol l^{-1} for ERM-CA400). The cleanliness of the BrCl solution was tested by a standard addition protocol every two days by adding known volumes of BrCl to a pre-purged Hg-free sample.

Laboratory mercury measurements

The MeHg samples were collected in 380 ml PFA bottles, acidified to 0.4% v/v HCl, and stored until analysis. Samples for MeHg and MMHg were analyzed on land within six months of sampling (**Text S1**). Both organic species were measured via a gas chromatography sector field inductively coupled plasma mass spectrometer (GC-SF-ICP-MS) and quantified by isotopic dilution [26,29,30]. Briefly, 140 ml narrow-mouth glass vials (VWR) were muffled at 450 °C for 4 hours to remove Hg traces. Approximately 110 ml sample was transferred to the 140 ml glass vial. Isotopically enriched spikes were added at an excess ratio of 5.1 for $i^{199}Hg$ and 4.2 for $MM^{201}Hg$ (ICS, Spain). The samples were left to equilibrate overnight. Afterward, a sodium acetate buffer solution (ULTREX II Ultrapure Reagent, J.T. Baker) was added, and the pH was adjusted to 3.9 with NH_3 (ULTREX II Ultrapure Reagent, J.T. Baker). The pH adjustment was followed by adding a 5% v/v tetrapropylborate solution (Merseburger Spezialchemikalien) and 150 µl isooctane (Sigma Aldrich). Subsequently, the bottles were sealed with a Teflon-lined crimp cap (Fisherbrand) and shaken for 15 minutes on an orbital shaker (Edmund Buhler KS15). The organic phase containing the derivatized Hg was recovered into vials for injection on a GC (THERMO GC 1300 with GC220 transfer module) coupled to a SF-ICP-MS (Thermo Element XR) system. The detection limit was 0.001 pmol l^{-}

[1] as a 3:1 signal-to-noise ratio. The theoretical concentration of 96.6± 7.9% of the spike was tested by reverse isotopic dilution in MeHgCl standard (Brooks Rand) traceable to NIST1641E.

The tHg concentration in the phytoplankton, sediment traps, and sediments was determined by cold vapor atomic absorption spectrometry (CV-AAS) according to the U.S. EPA method 7473. Between 70 and 140 mg of homogenized phytoplankton, 8 to 15 mg of material from the sediment trap, and 30 to 80 mg of sediment were placed separately in a pre-cleaned nickel vessel. The vessel with the sample was introduced into a Direct Mercury Analyzer (DMA-80 evo) and thermally decomposed. The products, including Hg, were transported by a Hg-free oxygen flow. The tHg was then selectively trapped by gold amalgamation, heated, desorbed, and detected by CV-AAS. The instrument was calibrated with NIST-3133 certified standard solution and verified daily against the fish protein certified reference material DORM-4 (certified concentration of 412 ± 36 ng g^{-1}, National Research Council of Canada) for phytoplankton, and the marine sediment certified reference material MESS-4 (certified concentration of 90 ± 40 ng g^{-1}, National Research Council of Canada) for sediment and sediment trap measurement. Instrument drift was controlled by standard bracketing every five samples using DORM-4 or MESS-4. Chlorophyll a was measured using the High-Performance Liquid Chromatography (HPLC) method. A volume of 2.8 L of seawater was collected and filtered through combusted 25 mm GF/F. The filters were then stored in liquid nitrogen for laboratory analysis. The samples were extracted and analyzed between 22 June and 2 July 2020. The extracts were analyzed using a complete Agilent Technologies system, and all peaks were identified based on retention time and spectral matches with pigment spectra obtained from liquid standards (DHI, Denmark) [31]. Chlorophyll-a has been used to proxy phytoplankton biomass by integrating it over the surface and intermediate layers (0 to 400 m depth) at each station.

According to the tHg concentrations detected in the samples, approximately 0.5 to 2 g of each sediment and sediment trap was pre-concentrated for Hg isotope ratio measurement using

the dual combustion-trapping method [32]. Released volatilized Hg^0 was trapped with 4 ml of 40% v/v double-distilled acid (2 HNO_3/1 HCl). Procedural blanks and certified reference materials (MESS-4) were processed with the samples following the same protocol. The trapped solutions were diluted with ultrapure water (18 MΩ cm, MQ) to Hg concentrations of 0.5 -1 ng g^{-1}, continuously mixed with $SnCl_2$ solution, and then were measured for Hg isotope ratios by coupling a customized cold vapor generation system to multi-collector inductively coupled plasma mass spectrometry (MC-ICP-MS, Neptune Plus at Tianjin University, China). Instrumental mass bias was corrected by both an internal NIST 997 Tl standard solution (supplied via Aridus II desolvation nebulizer system) using the exponential fractionation law and NIST 3133 Hg standard-sample bracketing method [33]. Hg isotope ratio is expressed as δ^{xxx}Hg (‰, xxx = 199, 200, 201, 202) by normalizing to a common NIST 3133 Hg standard:

$$\delta^{xxx}Hg\ (‰) = \left[\frac{(^{xxx}Hg/^{198}Hg)_{sample}}{(^{xxx}Hg/^{198}Hg)_{NIST3133}} - 1\right] \times 1000$$

Equation 1

MIF value is denoted as Δ^{xxx}Hg (‰, xxx = 199, 200, 201), representing the difference between the measured δ^{xxx}Hg value and that predicted from δ^{202}Hg using the kinetic MDF law [34]:

$$\Delta^{xxx}Hg\ (‰) = \delta^{xxx}Hg - {}^{xxx}\beta \times \delta^{202}Hg$$

Equation 2

Where the mass-dependent scaling factor $^{xxx}\beta$ is 0.2520 for ^{199}Hg, 0.5024 for ^{200}Hg, and 0.7520 for ^{201}Hg[34].

Isotope compositions of the secondary standard NIST-8610 solution and procedural certified reference materials (MESS-4) analyzed during different analytic sessions agreed with those reported in previous studies [20,34]. The samples' typical 2 SD analytic uncertainties were estimated as the larger 2 SD uncertainties of Hg isotope values in NIST-8610 or MESS-4. The 2 SD uncertainties of Hg isotope values in samples with replicate analyses were applied as

the analytic uncertainties only when they were larger than the typical 2 SD analytic uncertainties.

Vertical eddy diffusivity measurements and tHg vertical flux estimate

Microstructure measurements were done above the Panamax volcano using the vertical microstructure profiler VMP250 (Rockland Scientific). Detailed descriptions of the methods have been reported previously [28]. The profiler was equipped with microstructure sensors, two shear sensors, two temperature sensors, and Sea-Bird temperature and conductivity sensors. The dissipation rate of turbulent kinetic energy (epsilon) was estimated by shear measurements at a centimeter scale in four profiles [35]. Epsilon was then used to calculate vertical eddy diffusivity as:

$$K_z = Gamma\ x\ epsilon\ N^{-2}$$

Equation 3

Where gamma is a mixing efficiency calculated as the ratio between the buoyancy flux and the dissipation rate, and N is the buoyancy frequency. The tHg vertical supply above the Panamax volcano was calculated for each depth based on turbulent diffusive flux as

$$F = -K_z\ x\ \frac{d_{tHg}}{d_z}$$

Equation 4

The vertical eddy diffusivity (K_z) in the reference station (station 8) was estimated from CTD measurements (see Bonnet et al., 2023) with a validation of the same protocol compared to actual measurement of Kz at Station 5.

Sedimentation and mass accumulation rates

Sedimentation accumulation rates of the cores collected during the expedition have been previously reported [36]. Briefly, in the laboratory, ^{210}Pb and ^{226}Ra were performed on 4 to 10 g dried sediment using a semi-planar germanium detector for gamma spectroscopy (EGSP 2200-25-R, EURYSIS Mesures, [37]. Calibration of the gamma detector was achieved using certified reference material (IAEA: RGU, IAEA-314), activities are expressed in $mBq.g^{-1}$, and errors are based on 1 SD counting statistics. ^{210}Pb ($^{210}Pb_{xs}$) data was calculated by subtracting the activity supported by the parent isotope ^{226}Ra. The sedimentation rates were calculated from $^{210}Pb_{xs}$ profiles using the constant flux-constant sedimentation (CFCS) model [38]:

$$[^{210}Pb_{xs}]_z = [^{210}Pb_{xs}]_0 exp(-z\frac{\lambda}{SAR})$$

Equation 5

where $[^{210}Pb_{xs}]_0$ and $[^{210}Pb_{xs}]_z$ are the activities of excess ^{210}Pb at the water-sediment interface or the base of the mixed layer, and at depth z, λ is the decay constant of ^{210}Pb ($0.0311\ yr^{-1}$), and SAR is the sedimentation accumulation rate. The cumulative mass depth obtained from the core depth and the dry bulk density were used to express the mass accumulation rate. Dry bulk density was measured by determining the weight after drying (60 °C) of a known volume of wet sediment. Hg_p burial fluxes were calculated from sediment Hg_p concentration and mass accumulation rates.

Vent fluid dilution calculation

The dilution factor from the end-member vent fluid to the GoFLO collected plume waters was calculated using *Equation 6* [39,40]. This method accounts for the conservative mixing of Mn between the vent fluid end-member and seawater, allowing us to estimate the extent of dilution. Since Hg was measured in the same samples, we assume it follows the same dilution

process. This correction is essential for determining the true Hg concentration in the vent fluid end-member.

$$\text{Dilution Factor} = \frac{[Mn]_e - [Mn]_o}{[Mn]_s - [Mn]_o}$$

Equation 6

Where the subscripts *e*, *o,* and *s* indicate end-member (6.77 ± 0.4 mmol l^{-1} [41]), background Pacific Ocean seawater concentration (0.256 nmol l^{-1} [28]), and plume sample (Panamax highest Mn concentration 110 nmol l^{-1}) respectively.

Results and discussion

Seawater Hg concentrations along the cruise transect

Including all sampled main stations and depths, the median Hg concentrations are 1.00 pmol l^{-1} for tHg (n = 368), 0.278 pmol l^{-1} for DGM (n = 163), 0.260 pmol l^{-1} for MeHg (n = 218), 0.178 pmol l^{-1} for MMHg (n = 128), 0.111 pmol l^{-1} for DMHg (n = 122), and 0.208 pmol l^{-1} for Hg^0 (n = 89) (**Figure 1, Figure S1, Figure S2, Figure S3**). The Melanesian waters (stations 1, 2, and 3) display the highest median tHg concentrations (1.21 pmol l^{-1}, n = 54) (**Figure 1. b, Figure S1**). The South Pacific Gyre waters (stations 6, 7, and 8) have the lowest median tHg concentrations (0.869 pmol l^{-1}, n = 54) (**Figure 1. b, Figure S1**). The median tHg concentrations in the Lau Basin (stations 4, 11, and 12, 0.993 pmol l^{-1}, n = 66) and the Tonga Arc (stations 5 and 10, 0.970 pmol l^{-1}, n = 190) are between the elevated tHg concentrations of the Melanesian waters and the low tHg concentrations of the South Pacific Gyre (**Figure 1. b, Figure S2**). We constructed a database of reported tHg and MeHg in the Pacific Ocean (**Figure S4, Table S2**). The median tHg concentration in the Pacific Ocean is 0.820 pmol l^{-1}, in agreement with the median tHg concentrations measured in the South Pacific Gyre waters but lower than the median tHg concentrations measured in the Melanesian waters, the Lau Basin, and the Tonga Arc. Higher tHg concentrations than the reported Pacific Ocean values are observed at discrete depths in the Tonga Arc (up to 2.91 pmol l^{-1} in station 10) and station 4 (up to 2.47 pmol l^{-1}), located in the Lau Basin in the proximity of the Tonga Arc (**Figure S4**). The MeHg concentrations are lower in the surface waters along the transect (median 0.112 pmol l^{-1}, n = 112, depth < 500 m) than in deep waters (median 0.439 pmol l^{-1}, n = 106, depth > 500 m) in agreement with the distribution of the water masses (**Text S2**). We also find an enrichment of MeHg and DMHg concentrations between 500 and 1,000 m depth in the Lau Basin, the Tonga Arc, and station 3 near the Lau Basin in the Melanesian waters (**Figure 1. c**). At these depths, MeHg concentrations exceed 0.7 pmol l^{-1} (**Figure 1. c**), and MeHg is the

dominant Hg species (MeHg: 60 and 90%, **Figure 1.d**). Concentrations of DMHg reach 0.432 pmol l^{-1} at station 10 and 0.644 pmol l^{-1} in station 3 close to the Lau Basin (**Figure 1. e**). The high tHg, MeHg, and DMHg concentrations observed in the Lau Basin and the Tonga arc may result from contributions of hydrothermally derived Hg. The high tHg concentrations observed in the Melanesian waters may be influenced by inputs from the surrounding islands, coupled with far-reaching hydrothermal contributions from the Lau Basin and Tonga Arc, as previously observed for Fe [42].

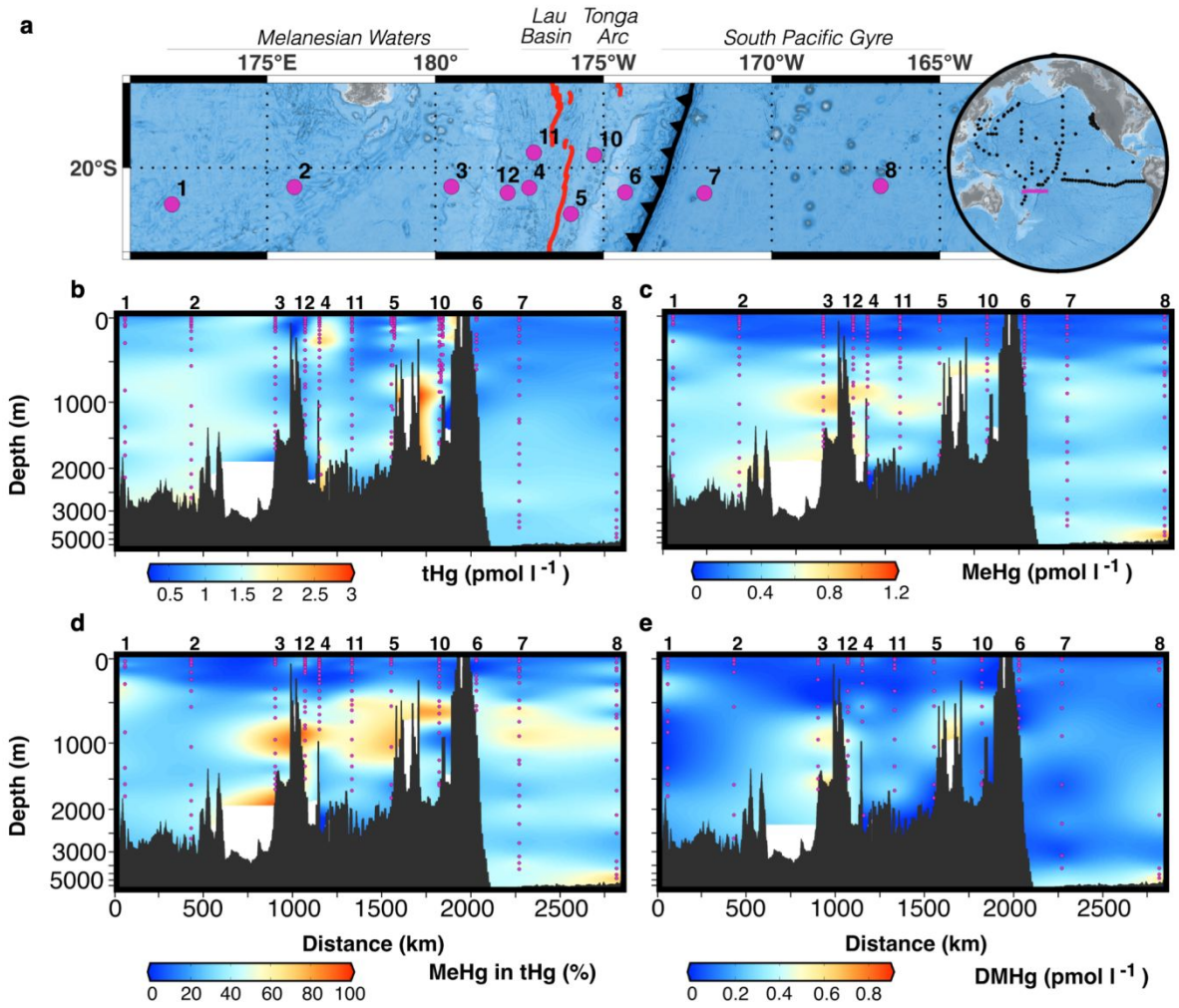

Figure 1. Overview of sampled main stations and Hg concentrations for selected species. ***a****, Sampled main stations from the Melanesian waters to the South Pacific Gyre in pink circles. The axis of the back-arc spreading center is shown in a continuous red line with arrows. The subduction zone is shown in a continuous black line with triangles [24]. To the right, the global map shows literature data of Pacific Ocean tHg and MeHg in black circles* (**Extended data Fig 4, Extended data Tab 1**)*. The pink continuous line shows the cruise transit. Underlying bathymetry from GEBCO. Maps created with QGIS.* ***b****, Measured tHg concentrations.* ***c****, Measured MeHg*

concentrations. ***d****, Percentage of MeHg in tHg.* ***e****, Calculated DMHg concentrations. Oceanographic sections constructed with ODV.*

Hydrothermal and volcanic Hg emissions at the Tonga Arc

Detailed surveys were performed at nine substations along stations 5 and 10 in the Tonga Arc, located 200 km apart (**Figure 1. a**), to test if the measured high concentrations of tHg, MeHg, and DMHg correspond to hydrothermal inputs. Bathymetry surveys revealed volcanic edifices at both stations, hereafter referred to as Panamax (station 5: 21°09'S; 175°45'W, ~200 m depth) [28] and Simone (station 10: 19°24'S; 175°03'W, ~300 m depth). Samples for Hg measurements were collected as full water column profiles and tow-yo casts focused on the maximum turbidity at both volcanoes. Fluid venting was detected at Panamax during the ship-borne acoustic survey, rising from the seafloor to 20 m below the sea surface [28]. A turbidity maximum was identified at 170 m in Panamax. Samples collected at Panamax display tHg concentrations varying from 0.401 to 10.5 pmol l^{-1} (n = 98). The highest tHg concentrations occur in the Panamax plume with values between 2.87 and 10.5 pmol l^{-1} (n = 5). The tHg concentrations remain high within the first 50 m above the volcano, decreasing rapidly above (**Figure 2. a**). The tHg anomalies at Panamax coincide with low pH (6.97 - 7.03) and a local dissolved oxygen (O_2) minimum (165 - 166 µmol l^{-1}) (**Figure S5. a**). Significant redox potential (Eh as low as -691.5 mV) and turbidity anomalies, together with high concentrations of dissolved CH_4 (up to 104 nmol l^{-1}), dissolved manganese (dMn up to 110 nmol l^{-1}), and dissolved iron (dFe up to 48.5 nmol l^{-1}), corroborate the hydrothermal origin of the tHg anomalies (**Figure S5. a**) [28,42]. The Panamax plume displays elevated DGM concentrations (up to 0.525 pmol l^{-1}), reaching values twice the median concentrations generally observed in the Pacific Ocean (**Figure 2. c**).

A turbidity maximum was also identified at the Simone volcano, between 260 and 310 m depth. The tHg concentrations around Simone volcano vary from 0.604 to 22.7 pmol l^{-1} (n = 92). The

highest tHg concentrations occur in the surrounding waters of Simone (**Figure 2. b**). The high tHg concentrations are associated with variable pH (7.90 - 8.46) and high concentrations of dissolved CH_4 (up to 35.8 nmol l^{-1}) (**Figure S5. b**). Like Panamax, the DGM concentrations at the Simone plume exceed the median concentrations measured along the transect (up to 0.354 pmol l^{-1}) (**Figure 2. d**). However, the ship-borne acoustic surveys at Simone did not indicate active hydrothermal venting. The observed tHg and DGM anomalies may instead result from the Metis Shoal volcano, which erupted one month before the cruise, forming a 21,000 m^2 island. The volcanic influence at Simone is further supported by the CTD data of a station located between Simone and the Metis Shoal volcano (ProvNox: 19°16'S; 174°54'W, 19 km from Simone, and 10 km from Metis Shoal), where tHg concentrations reach up to 6.80 pmol l^{-1} at 369 m depth (**Figure S2. f**).

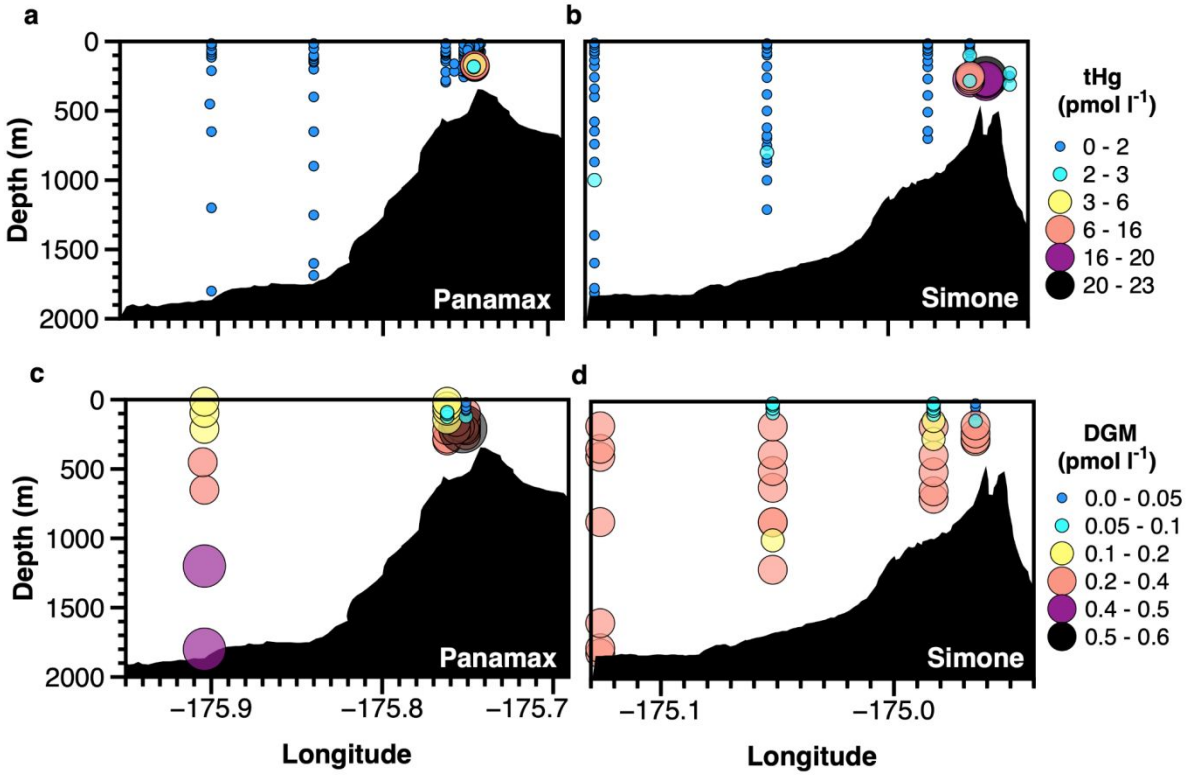

Figure 2. Measured Hg concentrations at substations along Panamax (station 5) and Simone volcanoes (station 10). ***a****, tHg concentrations in Panamax.* ***b****, tHg concentrations in Simone.* ***c****, DGM concentrations in Panamax.* ***d****, DGM concentrations in Simone. Concentrations in color and size scheme.*

Our observations indicate that the waters surrounding the Tonga Arc volcanoes are enriched in tHg up to 20 times above typical Pacific Ocean concentrations (**Figure S4**). The measured tHg concentrations above Panamax (up to 10.5 pmol l^{-1}) are in the same order of magnitude as the values reported in two individual plume samples at volcano TA25 (between 5 and 10 pmol l^{-1}), located 400 km south of Panamax in the Tonga Arc [17]. We used Mn to determine the degree of dilution of our plume samples relative to the vent fluid end-member. Due to its slow oxidation rate, Mn can serve as a conservative tracer to monitor vent fluid dilution in hydrothermal plumes [40,43,44]. The average Mn vent fluid end-member concentration in the Tonga Arc volcanoes is 6.77 ± 0.4 mmol l^{-1} [41]. The highest Mn concentration measured in the plume samples is 110 nmol l^{-1} (**Figure S5. a**). In contrast, the average Mn concentration in non-hydrothermal South Pacific Gyre waters (station 8) is 0.256 nmol l^{-1} [28]. Using a simple dilution model with these values, we estimate that our plume samples are diluted 55,831 times, and the pure vent fluid end-member would have tHg concentrations as high as 584,554 pmol l^{-1}. This estimate is higher than typically reported vent fluid tHg concentrations of up to 26,000 pmol l^{-1} [9,17,45–50], but in the same order as the highest reported vent fluid tHg concentration in the arc system of Panarea (248,766 pmol l^{-1}) [51]. Elemental Hg droplets have been observed further south of the same arc system at a shallow depth (200 m) [52], indicating that high enrichment of the vent fluids in the arc is likely. Hydrothermal deposits beneath the seafloor in the nearby Lau Basin show high Hg levels, suggesting that a part of Hg is retained locally [41].

The fate of hydrothermal Hg

To assess the impact of the Hg-enriched hydrothermal plume of Panamax in the water column, we estimated the tHg vertical supply to the surface waters (**Figure 3**). We compared the vertical supply from Panamax to that observed at station 8 in the South Pacific Gyre waters, which served as a reference for a non-hydrothermal oceanic station (**Figure S6**). At the depth of the primary acoustic anomaly of Panamax (170 m), the calculated tHg diffusive flux is 4,763

pmol m^{-2} d^{-1} (**Figure 3, Figure S6**). As tHg diffuses upwards, the flux decreases. The calculated diffuse flux remains high (up to 17.4 pmol m^{-2} d^{-1}) at 60 m depth in the photic layer where phytoplankton thrive, as observed with the chlorophyll-a data (**Figure 3, Figure S6**). In contrast, the calculated tHg diffusive flux is lower than 2 pmol m^{-2} d^{-1} at all depths in the South Pacific Gyre waters (**Figure S6**).

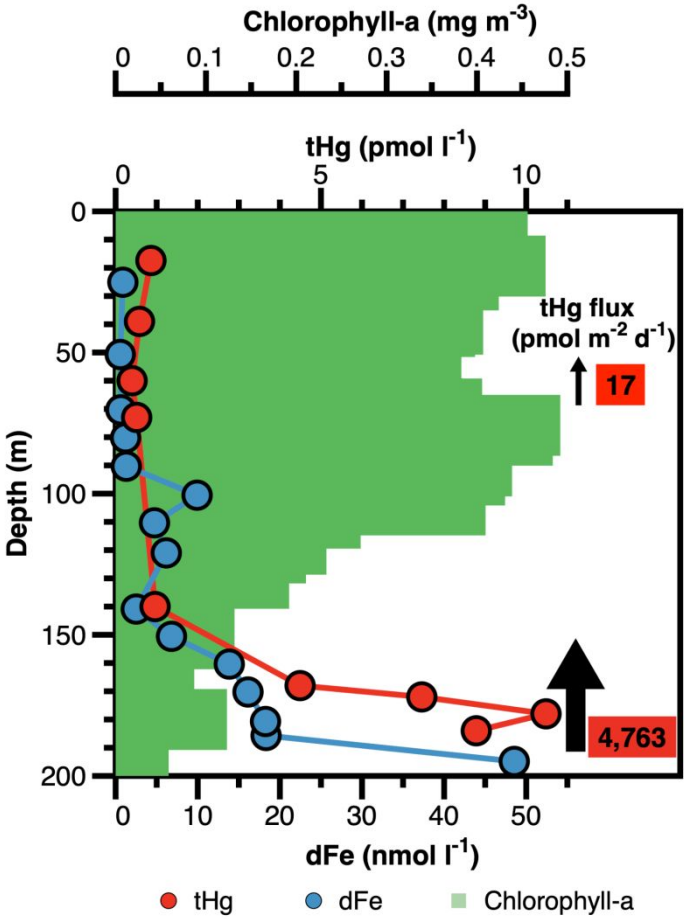

Figure 3. Hydrothermal inputs at Panamax volcano. *Hg and Fe concentrations and fluxes from the volcanic release point to the surface waters where most of the biomass, indicated by chlorophyll-a, resides.*

The integrated total chlorophyll-a shows that the highest phytoplankton biomass is found at stations 5 and 10 in the Tonga Arc, where Panamax and Simone volcanoes are located (**Figure 4**). The elevated biomass may be driven by the released Fe-rich hydrothermal fluids (**Figure 3, Figure S5**). The Fe input alleviates nutrient deficiency in the area, sustaining phytoplankton blooms that prevail six months of the year [28]. Concentrations of tHg in

phytoplankton were analyzed along the transect to assess the potential influence of the hydrothermal and volcanic input. The phytoplankton tHg concentrations vary from 1.25 to 11.6 ng g^{-1} dry weight (dw) (**Figure 4**). The found tHg concentrations in phytoplankton fall at the lower end of previously reported values of similar size fractions [12,53,54]. Phytoplankton at the Tonga Arc volcanic stations display low tHg concentrations (3.91 ng g^{-1} dw in station 5 and 2.44 ng g^{-1} dw in station 10, **Figure 4**) despite the hydrothermal and volcanic inputs. This pattern may be explained by biodilution, a process where Hg is diluted across a larger pool of cells, reducing individual cellular burdens [55–57]. The high tHg concentrations in the surrounding waters of stations 5 and 10 (**Figure 4. a**) may be diluted by the high biomass in these volcanic areas (**Figure 4. c**) and promote the low measured tHg concentrations in phytoplankton (**Figure 4. d**). The tHg concentrations in phytoplankton are lowest in the South Pacific Gyre waters (1.26 ng g^{-1} dw in station 7 and 1.50 ng g^{-1} dw in station 8), which is expected given the absence of Hg sources in this open ocean area (**Figure 4. d**). The highest tHg concentrations in phytoplankton are found in stations 4 (11.6 ng g^{-1} dw) and 11 (9.34 ng g^{-1} dw) in the Lau Basin (**Figure 4. d**). Elevated tHg concentrations in phytoplankton in the Lau Basin may result from the oxidation of Hg^0 to the more bioavailable Hg^{2+} during transport from the Tonga Arc. However, Hg^0 concentrations are not significantly different between the Tonga Arc and the Lau Basin (**Figure S7**). Instead, the elevated Hg in phytoplankton may be linked to reduced hydrothermal-derived Fe in the area [42], reducing the phytoplankton biomass (**Figure 4. b**), and decreasing the potential for biodilution of hydrothermal Hg from the distant Tonga Arc.

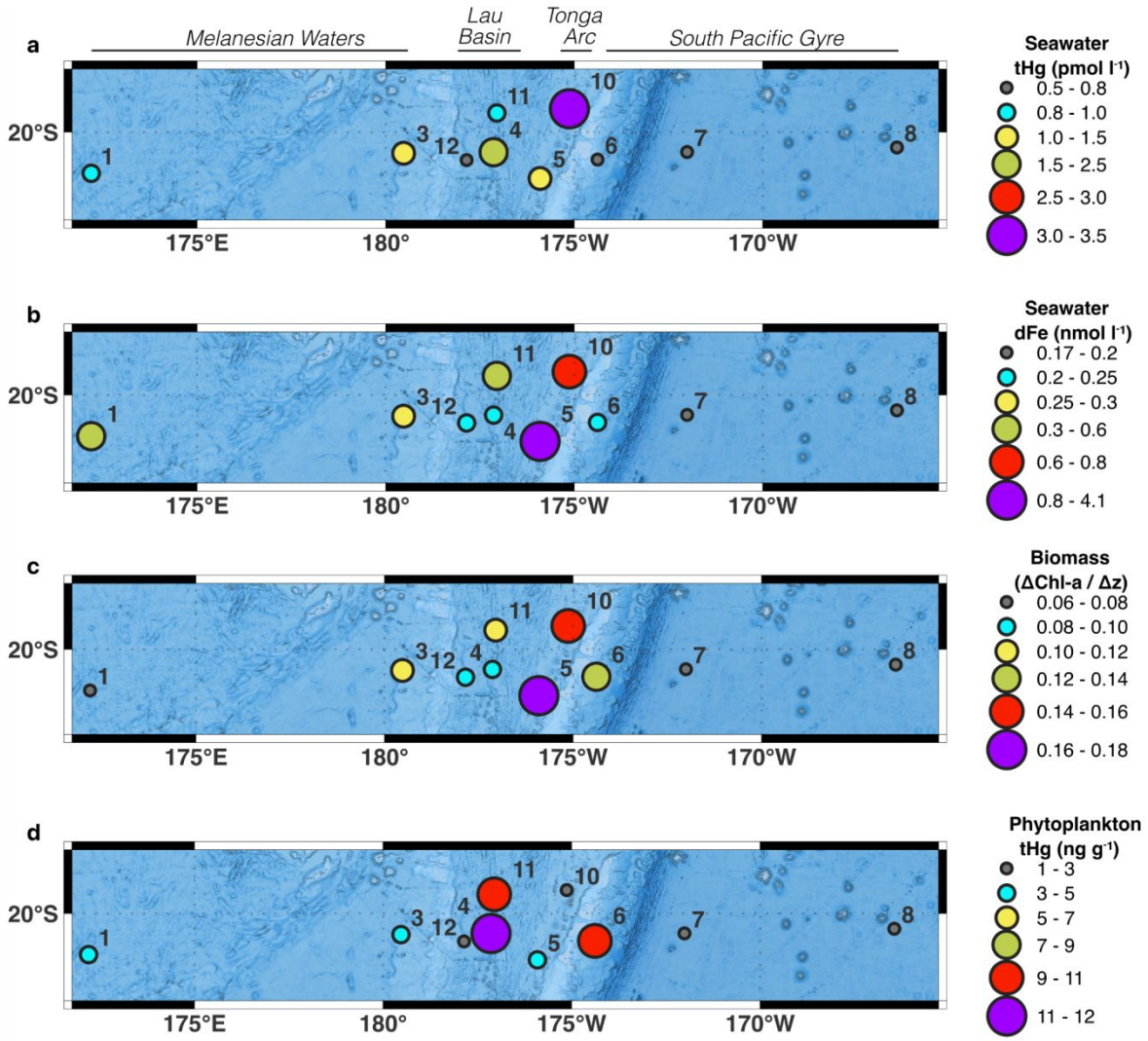

***Figure 4. Phytoplankton and chlorophyll-a data. a**, Average tHg concentrations in seawater in the upper 400 m including main stations and substations. **b**, Average dFe concentrations in seawater in the upper 400 m. **c**, Phytoplankton biomass as the integration of chlorophyll-a over 0 - 400 m depth. **d**, tHg concentrations in phytoplankton dry weight. Concentrations in color and size scheme. Underlying map showing bathymetry from GEBCO. Figures constructed using Qgis.*

To test whether hydrothermal-derived Hg from the Tonga Arc reaches the Lau Basin, promoting the elevated tHg in phytoplankton in the area, we deployed sediment traps at 200 m and 1,000 m depth. These traps were placed at station 12 in the Lau Basin, located in the main flow trajectory determined by profiling floats [42]. The yearly average Hg concentration is

79.1 ng g^{-1} in the 200 m sediment trap and 102.6 ng g^{-1} in the 1,000 m sediment trap. The average particle Hg (Hg_p) flux is 6.72 pmol m^{-2} d^{-1} for the 200 m sediment trap and 9.98 pmol m^{-2} d^{-1} for the 1000 m sediment trap (**Figure S8**). The average Hg_p fluxes of our traps are higher than the modeled Hg_p flux for non-hydrothermally affected areas in the Subtropical Pacific Ocean (4.5 pmol m^{-2} d^{-1}) [58]. The 200 m trap generally displays homogeneous Hg_p flux over the one-year mooring (**Figure S8**). The 1000 m trap has variable Hg_p flux, with the highest fluxes reaching 47.3 pmol m^{-2} d^{-1}. The highest fluxes of the 1000 m trap coincide with hydrothermal and volcanic signatures [59], such as elevated concentrations of lithogenic silica, copper, cobalt, nickel, and higher Fe/Al ratios (**Figure S8**). The differences in Hg_p fluxes between the 200 and 1000 m sediment traps may be explained by the fact that most volcanoes in the area are situated at depths greater than 200 m [22–24]. The isotopic signatures of particles sampled by sediment traps (200 m, $\Delta^{199}Hg$ = 0.21 ± 0.04 ‰; 1000m, $\Delta^{199}Hg$ = 0.28 ± 0.04 ‰; 2 SD) fall between the $\Delta^{199}Hg$ signature of non-hydrothermally derived deep ocean sediments ($\Delta^{199}Hg$ = 0.35 ‰) [60] and hydrothermal material ($\Delta^{199}Hg$ = 0.02 ‰) [48] further reflecting the hydrothermal and volcanic contributions to the traps and to the Lau Basin stations (**Figure S8**).

Sinking particles are remineralized, with only a small fraction reaching the deep ocean sediments [61]; during this process, part of the Hg is released, but some remain bound to particles. Sediment cores were collected at stations 5 and 10 in the Tonga Arc and 12 in the Lau Basin to quantify the burial of hydrothermal Hg. The Hg_p concentrations of the upper centimeter of the cores are 35 ng g^{-1} at station 5, 19.9 ng g^{-1} at station 10, and 48.3 ng g^{-1} at station 12. The cores show Hg_p concentrations in the typical range of deep ocean sediments (38 ± 21 ng g^{-1}) [62]. The Hg_p burial fluxes were calculated using ^{210}Pb dating [38]. Burial fluxes are 181 pmol m^{-2} d^{-1} at station 5, 81.5 pmol m^{-2} d^{-1} at station 10, and 259 pmol m^{-2} d^{-1} at station 12. The Hg_p burial fluxes exceed previously reported values for the West Pacific Ocean (21 pmol m^{-2} d^{-1}) [62], likely reflecting the hydrothermal and volcanic inputs. However, given the tHg diffusive flux above Panamax (4,763 pmol m^{-2} d^{-1}) and the burial flux range (81.5 to 259 pmol

m^{-2} d^{-1}), only 1.71 - 5.43% of hydrothermal Hg is retained in the sediments of the Lau Basin and Tonga Arc. Hydrothermal and volcanic contributions are further supported by the Δ^{199}Hg signatures of the sediments (Δ^{199}Hg = 0.26 ± 0.07 ‰, 2 SD at station 10 and Δ^{199}Hg = 0.21 ± 0.06 ‰, 2 SD at station 12), similar to the material in sediment traps (**Figure S8. e**).

Implications at regional and global scales

Previous studies link hydrothermal activity to elevated Hg levels in phytoplankton [14–16] and biota [17–20]. Our findings demonstrate that hydrothermal and volcanic inputs from the Tonga Arc contribute to elevated seawater Hg concentrations. The Hg inputs are accompanied by Fe release, which is delivered directly to the photic layer, resulting in both Hg contamination and Fe fertilization of the local communities. The Fe fertilization stimulates phytoplankton blooms, distributing Hg across a larger number and volume of cells, and hence biodiluting tHg concentrations in phytoplankton. This process results in some of the lowest tHg levels ever recorded in phytoplankton. As Hg and Fe are transported westward toward the Lau Basin, Fe, which is both scavenged by particles and actively uptaken as a micronutrient [28,42] becomes depleted leading to smaller phytoplankton blooms. In contrast, once released from hydrothermal vents, Hg mostly dilutes, remaining in the water column for longer distances [9]. The distant Lau Basin has insufficient Fe to support biomass blooms and biodilute the hydrothermal Hg leading to higher tHg in the local phytoplankton (**Figure 5**).

The persistence and transport of Hg in this system provide an opportunity to estimate the global hydrothermal Hg flux from arc volcanoes. Using the highest tHg flux at Panamax (4,763 pmol m^{-2} d^{-1}) and the caldera area (7 x 4,5 km, about 4% of the total area), we estimate a local Hg flux of 0.035 t y^{-1}. However, acoustic anomalies were observed at various sites across the Panamax volcano area. If venting would occur throughout the entire area of the stratovolcano, the resulting flux would be 0.86 t y^{-1}. The geology of the Tonga Arc has been revised by combining remote predictive mapping techniques with satellite databases, magnetics, ship-

based multibeam bathymetry, gravity measurements, seafloor imaging, and sampling (**Text S3**) [24]. The total area of potentially active volcanic structures in the Tonga Arc is 12,143 km^2 [24]. Assuming 100% hydrothermal activity across this area, the total Hg input from the Tonga Arc is 4.23 t y^{-1}. The calculated hydrothermal Hg flux includes the 1,700 km length of the Tonga Arc [10]. Globally, submarine arc systems extend for approximately 22,000 km [63]. Assuming all arc volcanoes behave like Panamax and 100% hydrothermal activity, the maximum global Hg flux from arc volcanoes is estimated at 54.8 t y^{-1}. When combined with the mid-ocean ridges flux (1.7 - 64.7 t y^{-1}) [9], the maximum hydrothermal contribution to the oceanic Hg inventory is 120 t y^{-1}. Recent estimates suggest that the oceans receive between 4,300 and 7,800 t y^{-1} of Hg from atmospheric deposition [64], and between 893 and 1,224 t y^{-1} of Hg from riverine inputs [6]. Our proposed hydrothermal flux estimate, even at its maximum, represents only a minor contribution to the total oceanic Hg inputs. In addition, our results show that hydrothermal systems can naturally regulate Hg concentrations through interactions with other elements. These suggest hydrothermal systems are unlikely to pose a significant threat to humans, at least in open ocean areas like those studied here. Future studies should focus on hydrothermal systems in coastal and enclosed basins where natural dynamics are likely disrupted by anthropogenic inputs, and hydrothermal Hg impacts on harvested food webs may be more important.

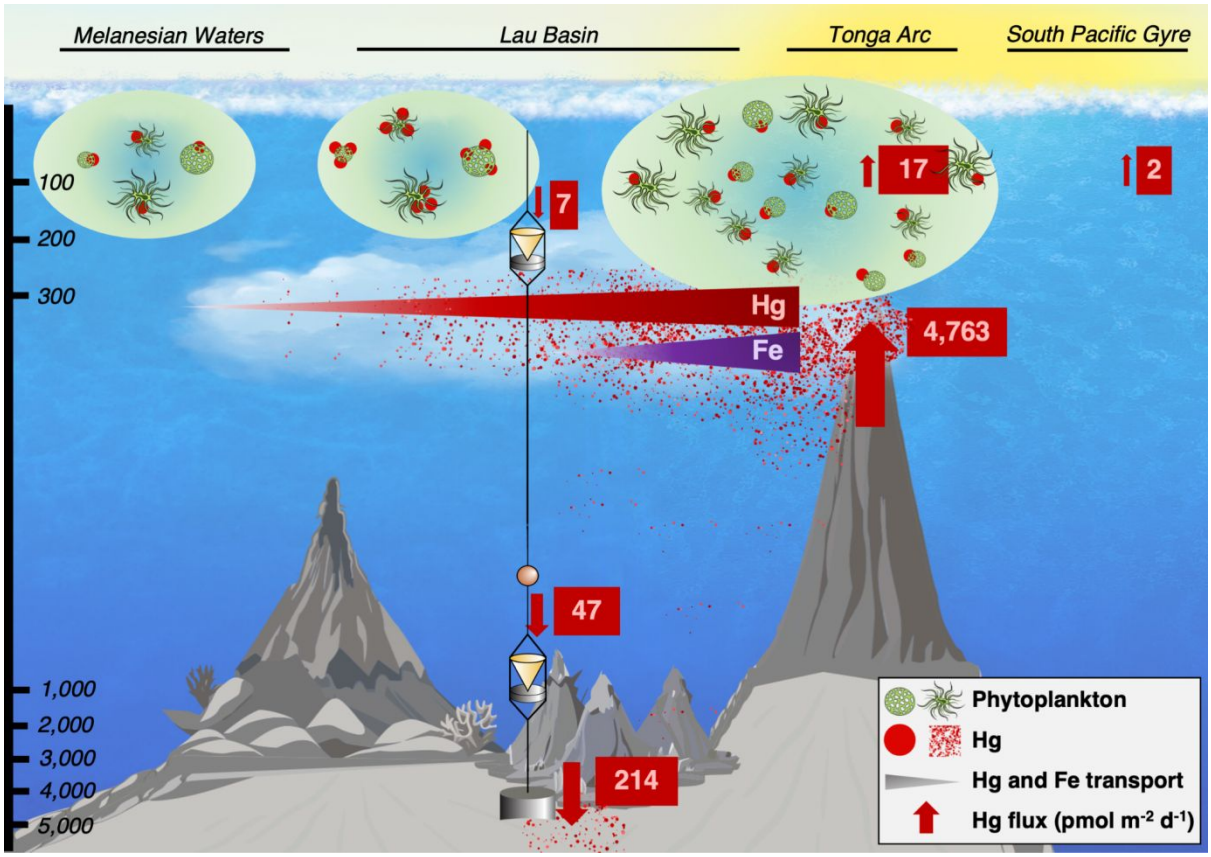

Figure 5. Schematic model of the impacts of the hydrothermal inputs to the surrounding areas. *Hg and Fe are released from the Tonga Arc volcanoes. The excess of Fe stimulates biological activity, causing phytoplankton blooms. Hydrothermal Hg is then diluted into the large pool of cells, resulting in phytoplankton with low Hg concentrations. Hg is transported in the hydrothermal plumes reaching the Lau Basin. Fe is transported for shorter distances than Hg. With a smaller biomass pool than the Tonga Arc, the excess of Hg in the Lau Basin cannot be diluted, leading to phytoplankton with elevated Hg concentrations. The transport of Hg from the Tonga Arc to the Lau Basin is supported by high Hg fluxes into the sediment traps and elevated burial fluxes.*

Supporting Information

Hg speciation definitions and calculations (Text S1, Table S1). Hg profiles along the cruise transect (Figures S1 and S2). Oceanographic sections of selected Hg species (Figure S3). Pacific Ocean database (Figure S4). Profiles of hydrothermal and volcanic parameters (Figure S5). tHg vertical diffuse flux (Figure S6). Phytoplankton and Chlorophyll-a data (Figure S7). Hg0 concentration data (Figure S8). Sediment traps data (Figure S9). Water masses analysis and Hg anomalies (Text S2). Geology of the study area (Text S3).

Acknowledgments

This project was supported by the French National Funding Agency (ANR) project HydrOThermal Mercury (ANR-21-CE34-0026), TONGA (ANR-18-CE01-0016), and MERTOX (ANR-17-CE34-0010). Funding for this project was also provided by the European Union's Horizon 2020 research and innovation program under the Marie Skłodowska-Curie GMOSTrain, grant agreement no. 860497. R.S. acknowledges the fund provided by the National Natural Science Foundation of China (42173011; 42373011). TONGA project and cruise was also supported by A-MIDEX grant TONGA (Excellence Initiative of Aix-Marseille University, a French "Investissements d'Avenir" program), Institut National des Sciences de l'Univers Les Enveloppes Fluides et l'Environnement grant TONGA, TGIR Flotte Océanographique Française TONGA cruise, the Institut de recherche pour le Développement (IRD). Sediment trap samples were processed by the "Cellule Pièges" methodology (INSU-CNRS: https://www.imev-mer.fr/web/?p=526). We thank Marie-Maëlle Desgranges for the sampling and her contribution to the mercury analyses. We thank Jean-Philippe Gac for contributing to the CH_4 analyses and sediment sampling. We thank Vincent Taillandier for acquiring all the CTD data. We thank Chloe Tilliette for her help and for providing files for the OMP analysis. We thank Nagib Bhairy for plankton sampling. We thank Celine Dimier and the SAPIGH platform of the Institut de la Mer de Villefranche (IMEV) for sampling on board and performing the pigment analyses. We thank Julian Torres Sanabria for the illustrations in Figure 4.

Corresponding author statement

Correspondence and requests for materials should be addressed to NTR, natalia.torres-rodriguez@mio.osupytheas.fr and LEHB, lars-eric.heimburger@mio.osupytheas.fr

Authors contributions statement

NTR contributed to conceptualization, analysis, and visualization and wrote the original draft. JY contributed to analysis, writing, reviewing, and editing. AD contributed to analysis and validation. IGA contributed to reviewing. IZ contributed to reviewing, editing, and statistical analysis. DP contributed to funding acquisition, reviewing, and editing. CB contributed to analysis, reviewing, and editing. JK contributed to reviewing and editing. MH contributed to funding acquisition, reviewing, and editing. DA contributed to reviewing and editing. SB contributed to conceptualization, investigation, funding acquisition, reviewing, and editing. CG contributed to conceptualization, investigation, funding acquisition, analysis, reviewing, and editing. RS contributed to reviewing and editing. LEHB contributed to conceptualization, analysis, investigation, funding acquisition, writing, visualization, reviewing, editing, and supervision.

Competing interest statement

The authors declare no competing interest.

Data statement

The data presented in this study has been submitted to GEOTRACES.

Present addresses

°JY: Department of Marine Sciences, University of Connecticut, Groton, Connecticut, 06340, United States

References

(1) Petrova, M. V.; Ourgaud, M.; Boavida, J. R. H.; Dufour, A.; Onrubia, J. A. T.; Lozingot, A.; Heimbürger-Boavida, L.-E. Human Mercury Exposure Levels and Fish Consumption at the French Riviera. *Chemosphere* **2020**, *258*, 127232. https://doi.org/10.1016/j.chemosphere.2020.127232.

(2) Al-Sulaiti, M. M.; Soubra, L.; Al-Ghouti, M. A. The Causes and Effects of Mercury and Methylmercury Contamination in the Marine Environment: A Review. *Curr. Pollut. Rep.* **2022**, *8* (3), 249–272. https://doi.org/10.1007/s40726-022-00226-7.

(3) Outridge, P. M.; Mason, R. P.; Wang, F.; Guerrero, S.; Heimbürger-Boavida, L. E. Updated Global and Oceanic Mercury Budgets for the United Nations Global Mercury Assessment 2018. *Environ Sci Technol* **2018**, *52* (20), 11466–11477. https://doi.org/10.1021/acs.est.8b01246.

(4) Qiu, X.; Liu, M.; Zhang, Y.; Zhang, Q.; Lin, H.; Cai, X.; Li, J.; Dai, R.; Zheng, S.; Wang, J.; Zhu, Y.; Shen, H.; Shen, G.; Wang, X.; Tao, S. Declines in Anthropogenic Mercury Emissions in the Global North and China Offset by the Global South. *Nat. Commun.* **2025**, *16* (1), 1179. https://doi.org/10.1038/s41467-025-56274-2.

(5) Bone, S. E.; Charette, M. A.; Lamborg, C. H.; Gonneea, M. E. Has Submarine Groundwater Discharge Been Overlooked as a Source of Mercury to Coastal Waters? *Environ. Sci. Technol.* **2007**, *41* (9), 3090–3095. https://doi.org/10.1021/es0622453.

(6) Liu, M.; Zhang, Q.; Maavara, T.; Liu, S.; Wang, X.; Raymond, P. A. Rivers as the Largest Source of Mercury to Coastal Oceans Worldwide. *Nat Geosci* **2021**, *14* (9), 672–677. https://doi.org/10.1038/s41561-021-00793-2.

(7) Strode, S. A.; Jaeglé, L.; Selin, N. E.; Jacob, D. J.; Park, R. J.; Yantosca, R. M.; Mason, R. P.; Slemr, F. Air-sea Exchange in the Global Mercury Cycle. *Glob. Biogeochem. Cycles* **2007**, *21* (1). https://doi.org/10.1029/2006gb002766.

(8) German, C. R.; Casciotti, K. A.; Dutay, J.-C.; Heimbürger, L. E.; Jenkins, W. J.; Measures, C. I.; Mills, R. A.; Obata, H.; Schlitzer, R.; Tagliabue, A.; Turner, D. R.; Whitby, H.

Hydrothermal Impacts on Trace Element and Isotope Ocean Biogeochemistry. *Philosophical Transactions Ser Math Phys Eng Sci* **2016**, *374* (2081), 20160035. https://doi.org/10.1098/rsta.2016.0035.

(9) Torres-Rodriguez, N.; Yuan, J.; Petersen, S.; Dufour, A.; González-Santana, D.; Chavagnac, V.; Planquette, H.; Horvat, M.; Amouroux, D.; Cathalot, C.; Pelleter, E.; Sun, R.; Sonke, J. E.; Luther, G. W.; Heimbürger-Boavida, L.-E. Mercury Fluxes from Hydrothermal Venting at Mid-Ocean Ridges Constrained by Measurements. *Nat. Geosci.* **2023**, 1–7. https://doi.org/10.1038/s41561-023-01341-w.

(10) Hannington, M. D.; Ronde, C. E. J. D.; Petersen, S. Sea-Floor Tectonics and Submarine Hydrothermal Systems. In *One Hundredth Anniversary Volume*; Society of Economic Geologists, **2005**; pp 111–141.

(11) Villar, E.; Cabrol, L.; Heimbürger-Boavida, L. Widespread Microbial Mercury Methylation Genes in the Global Ocean. *Environ. Microbiol. Rep.* **2020**, *12* (3), 277–287. https://doi.org/10.1111/1758-2229.12829.

(12) Tesán-Onrubia, J. A.; Heimbürger-Boavida, L.-E.; Dufour, A.; Harmelin-Vivien, M.; García-Arévalo, I.; Knoery, J.; Thomas, B.; Carlotti, F.; Tedetti, M.; Bănaru, D. Bioconcentration, Bioaccumulation and Biomagnification of Mercury in Plankton of the Mediterranean Sea. *Mar. Pollut. Bull.* **2023**, *194* (Pt B), 115439. https://doi.org/10.1016/j.marpolbul.2023.115439.

(13) Médieu, A.; Point, D.; Itai, T.; Angot, H.; Buchanan, P. J.; Allain, V.; Fuller, L.; Griffiths, S.; Gillikin, D. P.; Sonke, J. E.; Heimbürger-Boavida, L.-E.; Desgranges, M.-M.; Menkes, C. E.; Madigan, D. J.; Brosset, P.; Gauthier, O.; Tagliabue, A.; Bopp, L.; Verheyden, A.; Lorrain, A. Evidence That Pacific Tuna Mercury Levels Are Driven by Marine Methylmercury Production and Anthropogenic Inputs. *Proc. Natl. Acad. Sci.* **2022**, *119* (2), e2113032119. https://doi.org/10.1073/pnas.2113032119.

(14) Duarte, B.; Cabrita, M. T.; Vidal, T.; Pereira, J. L.; Pacheco, M.; Pereira, P.; Canário, J.; Gonçalves, F. J. M.; Matos, A. R.; Rosa, R.; Marques, J. C.; Caçador, I.; Gameiro, C. Phytoplankton Community-Level Bio-Optical Assessment in a Naturally Mercury

Contaminated Antarctic Ecosystem (Deception Island). *Mar. Environ. Res.* **2018**, *140*, 412–421. https://doi.org/10.1016/j.marenvres.2018.07.014.

(15) Hsiao, S.-H.; Fang, T.-H. Hg Bioaccumulation in Marine Copepods around Hydrothermal Vents and the Adjacent Marine Environment in Northeastern Taiwan. Mar. Pollut. Bull. **2013**, *74* (1), 175–182. https://doi.org/10.1016/j.marpolbul.2013.07.007.

(16) Tomiyasu, T.; Matsuki, H.; Oda, M.; Kodamatani, H.; Kanzaki, R.; Kobari, T. Impact of Mercury Discharged from Submarine Volcano on Inner Bay Ecosystems. Chemosphere 2023, *339*, 139748. https://doi.org/10.1016/j.chemosphere.2023.139748.

(17) Lee, S.; Kim, S.-J.; Ju, S.-J.; Pak, S.-J.; Son, S.-K.; Yang, J.; Han, S. Mercury Accumulation in Hydrothermal Vent Mollusks from the Southern Tonga Arc, Southwestern Pacific Ocean. Chemosphere **2015**, *127*, 246–253. https://doi.org/10.1016/j.chemosphere.2015.01.006.

(18) Martins, I.; Costa, V.; Porteiro, F.; Cravo, A.; Santos, R. S. Mercury Concentrations in Invertebrates from Mid-Atlantic Ridge Hydrothermal Vent Fields. *J. Mar. Biol. Assoc. United Kingd.* **2001**, *81* (6), 913–915. https://doi.org/10.1017/s0025315401004830.

(19) Demina, L. L.; Galkin, S. V. On the Role of Abiogenic Factors in the Bioaccumulation of Heavy Metals by the Hydrothermal Fauna of the Mid-Atlantic Ridge. *Oceanology* **2008**, *48* (6), 784–797. https://doi.org/10.1134/s0001437008060040.

(20) Yuan, J.; Liu, Y.; Chen, S.; Peng, X.; Li, Y.-F.; Li, S.; Zhang, R.; Zheng, W.; Chen, J.; Sun, R.; Heimbürger-Boavida, L.-E. Mercury Isotopes in Deep-Sea Epibenthic Biota Suggest Limited Hg Transfer from Photosynthetic to Chemosynthetic Food Webs. Environ. Sci. Technol. 2023, *57* (16), 6550–6562. https://doi.org/10.1021/acs.est.3c01276.

(21) Shiozaki, T.; Kodama, T.; Furuya, K. Large-scale Impact of the Island Mass Effect through Nitrogen Fixation in the Western South Pacific Ocean. *Geophys. Res. Lett.* **2014**, *41* (8), 2907–2913. https://doi.org/10.1002/2014gl059835.

(22) Lupton, J. E.; Pyle, D. G.; Jenkins, W. J.; Greene, R.; Evans, L. Evidence for an Extensive Hydrothermal Plume in the Tonga-Fiji Region of the South Pacific. *Geochem., Geophys., Geosystems* **2004**, *5* (1), n/a-n/a. https://doi.org/10.1029/2003gc000607.

(23) Massoth, G.; Baker, E.; Worthington, T.; Lupton, J.; Ronde, C. de; Arculus, R.; Walker, S.; Nakamura, K.; Ishibashi, J.; Stoffers, P.; Resing, J.; Greene, R.; Lebon, G. Multiple Hydrothermal Sources along the South Tonga Arc and Valu Fa Ridge. Geochem., Geophys., Geosystems **2007**, *8* (11). https://doi.org/10.1029/2007gc001675.

(24) Stewart, M. S.; Hannington, M. D.; Emberley, J.; Baxter, A. T.; Krätschell, A.; Petersen, S.; Brandl, P. A.; Anderson, M. O.; Mercier-Langevin, P.; Mensing, R.; Breker, K.; Fassbender, M. L. A New Geological Map of the Lau Basin (Southwestern Pacific Ocean) Reveals Crustal Growth Processes in Arc-Backarc Systems. *Geosphere* **2022**. https://doi.org/10.1130/ges02340.1.

(25) Bonnet, S.; Guieu, C.; Bruyant, F.; Prášil, O.; Wambeke, F. V.; Raimbault, P.; Moutin, T.; Grob, C.; Gorbunov, M. Y.; Zehr, J. P.; Masquelier, S. M.; Garczarek, L.; Claustre, H. Nutrient Limitation of Primary Productivity in the Southeast Pacific (BIOSOPE Cruise). *Biogeosciences* **2008**, *5* (1), 215–225. https://doi.org/10.5194/bg-5-215-2008.

(26) Kleindienst, A.; Živković, I.; Tessier, E.; Koenig, A.; Heimbürger-Boavida, L.-E.; Horvat, M.; Amouroux, D. Assessing Comparability and Uncertainty of Analytical Methods for Methylated Mercury Species in Seawater. *Anal. Chim. Acta* **2023**, *1278*, 341735. https://doi.org/10.1016/j.aca.2023.341735.

(27) Cutter, G. A.; Casciotti, K.; Croot, P.; Geibert, W.; Heimbürger, L.-E.; Lohan, M. C.; Planquette, H.; Flierdt, T. van de. Sampling and Sample-Handling Protocols for GEOTRACES Cruises, Version 3.0. **2017**.

(28) Bonnet, S.; Guieu, C.; Taillandier, V.; Boulart, C.; Bouruet-Aubertot, P.; Gazeau, F.; Scalabrin, C.; Bressac, M.; Knapp, A. N.; Cuypers, Y.; González-Santana, D.; Forrer, H. J.; Grisoni, J.-M.; Grosso, O.; Habasque, J.; Jardin-Camps, M.; Leblond, N.; Moigne, F. A. C. L.; Lebourges-Dhaussy, A.; Lory, C.; Nunige, S.; Pulido-Villena, E.; Rizzo, A. L.; Sarthou, G.; Tilliette, C. Natural Iron Fertilization by Shallow Hydrothermal Sources Fuels Diazotroph Blooms in the Ocean. *Science* **2023**, *380* (6647), 812–817. https://doi.org/10.1126/science.abq4654.

(29) Heimbürger, L.-E.; Sonke, J. E.; Cossa, D.; Point, D.; Lagane, C.; Laffont, L.; Galfond,

B. T.; Nicolaus, M.; Rabe, B.; Loeff, M. R. van der. Shallow Methylmercury Production in the Marginal Sea Ice Zone of the Central Arctic Ocean. *Sci Rep-uk* **2015**, 5 (1), 10318. https://doi.org/10.1038/srep10318.

(30) Monperrus, M.; Tessier, E.; Veschambre, S.; Amouroux, D.; Donard, O. Simultaneous Speciation of Mercury and Butyltin Compounds in Natural Waters and Snow by Propylation and Species-Specific Isotope Dilution Mass Spectrometry Analysis. *Anal. Bioanal. Chem.* **2005**, *381* (4), 854–862. https://doi.org/10.1007/s00216-004-2973-7.

(31) Ras, J.; Claustre, H.; Uitz, J. Spatial Variability of Phytoplankton Pigment Distributions in the Subtropical South Pacific Ocean: Comparison between in Situ and Predicted Data. Biogeosciences 2008, 5 (2), 353–369. https://doi.org/10.5194/bg-5-353-2008.

(32) Sun, R.; Enrico, M.; Heimbürger, L.-E.; Scott, C.; Sonke, J. E. A Double-Stage Tube Furnace—Acid-Trapping Protocol for the Pre-Concentration of Mercury from Solid Samples for Isotopic Analysis. Anal. Bioanal. Chem. **2013**, *405* (21), 6771–6781. https://doi.org/10.1007/s00216-013-7152-2.

(33) Shi, M.; Bergquist, B. A.; Zhou, A.; Zhao, Y.; Sun, R.; Chen, J.; Zheng, W. The Efficiency of Hg Cold Vapor Generation and Its Influence on Hg Isotope Analysis by MC-ICP-MS. *J. Anal. At. Spectrom.* **2023**, *38* (5), 1076–1087. https://doi.org/10.1039/d3ja00056g.

(34) Blum, J. D.; Bergquist, B. A. Reporting of Variations in the Natural Isotopic Composition of Mercury. Anal. Bioanal. Chem. **2007**, *388* (2), 353–359. https://doi.org/10.1007/s00216-007-1236-9.

(35) Bouruet-Aubertot, P.; Cuypers, Y.; Doglioli, A.; Caffin, M.; Yohia, C.; Verneil, A. de; Petrenko, A.; Lefèvre, D.; Goff, H. L.; Rougier, G.; Picheral, M.; Moutin, T. Longitudinal Contrast in Turbulence along a 19S Section in the Pacific and Its Consequences for Biogeochemical Fluxes. Biogeosciences **2018**, *15* (24), 7*485*–7504. https://doi.org/10.5194/bg-15-7485-2018.

(36) Tilliette, C.; Gazeau, F.; Portlock, G.; Benavides, M.; Bonnet, S.; Guigue, C.; Leblond, N.; Lory, C.; Marie, D.; Montanes, M.; Pulido-Villena, E.; Sarthou, G.; Tedetti, M.; Vorrath,

M.-E.; Whitby, H.; Guieu, C. Influence of Shallow Hydrothermal Fluid Release on the Functioning of Phytoplankton Communities. *Front. Mar. Sci.* **2023**, *10*, 1082077. https://doi.org/10.3389/fmars.2023.1082077.

(37) Schmidt, S.; Howa, H.; Diallo, A.; Martín, J.; Cremer, M.; Duros, P.; Fontanier, C.; Deflandre, B.; Metzger, E.; Mulder, T. Recent Sediment Transport and Deposition in the Cap-Ferret Canyon, South-East Margin of Bay of Biscay. *Deep Sea Res. Part II: Top. Stud. Oceanogr.* **2014**, *104*, 134–144. https://doi.org/10.1016/j.dsr2.2013.06.004.

(38) Robbins, J. A.; Edgington, D. N. Determination of Recent Sedimentation Rates in Lake Michigan Using Pb-210 and Cs-137. *Geochim. Cosmochim. Acta* **1975**, *39* (3), 285–304. https://doi.org/10.1016/0016-7037(75)90198-2.

(39) Fischer, H. B.; List, E. J.; Koh, R. C. Y.; Imberger, J.; Brooks, N. H. *Mixing in Inland and Coastal Waters*; BROOKS"], ["HUGO B. FISCHER and E. JOHN LIST and ROBERT C.Y. KOH and JÖRG IMBERGER and NORMAN H., Ed.; Academic Press: San Diego, 1979. https://doi.org/10.1016/b978-0-08-051177-1.50005-2.

(40) James, R. H.; Elderfield, H. Dissolved and Particulate Trace Metals in Hydrothermal Plumes at the Mid-Atlantic Ridge. *Geophys Res Lett* **1996**, *23* (23), 3*499*–3502. https://doi.org/10.1029/96gl01588.

(41) Fouquet, Y.; Stackelberg, U. von; Charlou, J. L.; Erzinger, J.; Herzig, P. M.; Muehe, R.; Wiedicke, M. Metallogenesis in Back-Arc Environments; the Lau Basin Example. *Econ Geol* **1993**, *88* (8), 2154–2181. https://doi.org/10.2113/gsecongeo.88.8.2154.

(42) Tilliette, C.; Taillandier, V.; Bouruet-Aubertot, P.; Grima, N.; Maes, C.; Montanes, M.; Sarthou, G.; Vorrath, M. -E.; Arnone, V.; Bressac, M.; González-Santana, D.; Gazeau, F.; Guieu, C. Dissolved Iron Patterns Impacted by Shallow Hydrothermal Sources Along a Transect Through the Tonga-Kermadec Arc. *Global Biogeochem Cy* **2022**, *36* (7). https://doi.org/10.1029/2022gb007363.

(43) Field, M. P.; Sherrell, R. M. Dissolved and Particulate Fe in a Hydrothermal Plume at 9°45'N, East Pacific Rise: Slow Fe (II) Oxidation Kinetics in Pacific Plumes. *Geochim Cosmochim Ac* **2000**, *64* (4), 619–628. https://doi.org/10.1016/s0016-7037(99)00333-6.

(44) González-Santana, D.; Planquette, H.; Cheize, M.; Whitby, H.; Gourain, A.; Holmes, T.; Guyader, V.; Cathalot, C.; Pelleter, E.; Fouquet, Y.; Sarthou, G. Processes Driving Iron and Manganese Dispersal From the TAG Hydrothermal Plume (Mid-Atlantic Ridge): Results From a GEOTRACES Process Study. *Frontiers Mar Sci* **2020**, *7*, 568. https://doi.org/10.3389/fmars.2020.00568.

(45) Roberts, H.; Pichler, T. Hg in the Hydrothermal Fluids and Gases in Baia Di Levante, Vulcano, Italy. *Mar Chem* **2022**, *244*, 104147. https://doi.org/10.1016/j.marchem.2022.104147.

(46) Roberts, H.; Price, R.; Brombach, C.-C.; Pichler, T. Mercury in the Hydrothermal Fluids and Gases in Paleochori Bay, Milos, Greece. Mar Chem **2021**, *233*, 103984. https://doi.org/10.1016/j.marchem.2021.103984.

(47) Bagnato, E.; Oliveri, E.; Acquavita, A.; Covelli, S.; Petranich, E.; Barra, M.; Italiano, F.; Parello, F.; Sprovieri, M. Hydrochemical Mercury Distribution and Air-Sea Exchange over the Submarine Hydrothermal Vents off-Shore Panarea Island (Aeolian Arc, Tyrrhenian Sea). Mar Chem **2017**, *194*, 63–78. https://doi.org/10.1016/j.marchem.2017.04.003.

(48) Sherman, L. S.; Blum, J. D.; Nordstrom, D. K.; McCleskey, R. B.; Barkay, T.; Vetriani, C. Mercury Isotopic Composition of Hydrothermal Systems in the Yellowstone Plateau Volcanic Field and Guaymas Basin Sea-Floor Rift. *Earth Planet Sc Lett* **2009**, *279* (1–2), 86–96. https://doi.org/10.1016/j.epsl.2008.12.032.

(49) Crespo-Medina, M.; Chatziefthimiou, A. D.; Bloom, N. S.; Luther, G. W. I.; Wright, D. D.; Reinfelder, J. R.; Vetriani, C.; Barkay, T. Adaptation of Chemosynthetic Microorganisms to Elevated Mercury Concentrations in Deep-sea Hydrothermal Vents. *Limnol Oceanogr* **2009**, *54* (1), 41–49. https://doi.org/10.4319/lo.2009.54.1.0041.

(50) Lamborg, C. H.; Damm, K. L. V.; Fitzgerald, W. F.; Hammerschmidt, C. R.; Zierenberg, R. Mercury and Monomethylmercury in Fluids from Sea Cliff Submarine Hydrothermal Field, Gorda Ridge. Geophys Res Lett **2006**, *33* (17). https://doi.org/10.1029/2006gl026321.

(51) Pichler, T. Environmental Inventory of Mercury (Hg) for the Marine Shallow Water Hydrothermal System at Panarea, Italy. *Sci. Total Environ.* **2024**, *911*, 168575.

https://doi.org/10.1016/j.scitotenv.2023.168575.

(52) Stoffers, P.; Hannington, M.; Wright, I.; Herzig, P.; Ronde, C. de; Party, S. S. Elemental Mercury at Submarine Hydrothermal Vents in the Bay of Plenty, Taupo Volcanic Zone, New Zealand. *Geology* **1999**, *27* (10), 931–934. https://doi.org/10.1130/0091-7613(1999)027<0931:emashv>2.3.co;2.

(53) Gosnell, K. J.; Mason, R. P. Mercury and Methylmercury Incidence and Bioaccumulation in Plankton from the Central Pacific Ocean. *Mar. Chem.* **2015**, *177*, 772–780. https://doi.org/10.1016/j.marchem.2015.07.005.

(54) Gosnell, K. J.; Balcom, P. H.; Tobias, C. R.; Gilhooly, W. P.; Mason, R. P. Spatial and Temporal Trophic Transfer Dynamics of Mercury and Methylmercury into Zooplankton and Phytoplankton of Long Island Sound. *Limnol. Oceanogr.* **2017**, *62* (3), 1122–1138. https://doi.org/10.1002/lno.10490.

(55) Karimi, R.; Chen, C. Y.; Pickhardt, P. C.; Fisher, N. S.; Folt, C. L. Stoichiometric Controls of Mercury Dilution by Growth. Proc. Natl. Acad. Sci. 2007, 104 (18), 7477–7482. https://doi.org/10.1073/pnas.0611261104.

(56) Hammerschmidt, C. R.; Finiguerra, M. B.; Weller, R. L.; Fitzgerald, W. F. Methylmercury Accumulation in Plankton on the Continental Margin of the Northwest Atlantic Ocean. Environ. Sci. Technol. 2013, 47 (8), 3671–3677. https://doi.org/10.1021/es3048619.

(57) Driscoll, C. T.; Chen, C. Y.; Hammerschmidt, C. R.; Mason, R. P.; Gilmour, C. C.; Sunderland, E. M.; Greenfield, B. K.; Buckman, K. L.; Lamborg, C. H. Nutrient Supply and Mercury Dynamics in Marine Ecosystems: A Conceptual Model. Environ. Res. **2012**, *119*, 118–131. https://doi.org/10.1016/j.envres.2012.05.002.

(58) Soerensen, A. L.; Mason, R. P.; Balcom, P. H.; Jacob, D. J.; Zhang, Y.; Kuss, J.; Sunderland, E. M. Elemental Mercury Concentrations and Fluxes in the Tropical Atmosphere and Ocean. Environ. Sci. Technol. 2014, 48 (19), 11312–11319. https://doi.org/10.1021/es503109p.

(59) Tilliette, C.; Gazeau, F.; Chavagnac, V.; Leblond, N.; Montanes, M.; Leblanc, K.; Schmidt, S.; Charrière, B.; Bhairy, N.; Guieu, C. Significant Impact of Hydrothermalism on

the Biogeochemical Signature of Sinking and Sedimented Particles in the Lau Basin. *J. Geophys. Res.: Oceans* **2023**, *128* (12). https://doi.org/10.1029/2023jc019828.

(60) Yin, R.; Feng, X.; Chen, B.; Zhang, J.; Wang, W.; Li, X. Identifying the Sources and Processes of Mercury in Subtropical Estuarine and Ocean Sediments Using Hg Isotopic Composition. Environ. Sci. Technol. 2015, 49 (3), 1347–1355. https://doi.org/10.1021/es504070y.

(61) Heimbürger, L.-E.; Cossa, D.; Thibodeau, B.; Khripounoff, A.; Mas, V.; Chiffoleau, J.-F.; Schmidt, S.; Migon, C. Natural and Anthropogenic Trace Metals in Sediments of the Ligurian Sea (Northwestern Mediterranean). *Chem. Geol.* **2012**, *291*, 141–151. https://doi.org/10.1016/j.chemgeo.2011.10.011.

(62) Hayes, C. T.; Costa, K. M.; Anderson, R. F.; Calvo, E.; Chase, Z.; Demina, L. L.; Dutay, J.; German, C. R.; Heimbürger-Boavida, L.; Jaccard, S. L.; Jacobel, A.; Kohfeld, K. E.; Kravchishina, M. D.; Lippold, J.; Mekik, F.; Missiaen, L.; Pavia, F. J.; Paytan, A.; Pedrosa-Pamies, R.; Petrova, M. V.; Rahman, S.; Robinson, L. F.; Roy-Barman, M.; Sanchez-Vidal, A.; Shiller, A.; Tagliabue, A.; Tessin, A. C.; Hulten, M. van; Zhang, J. Global Ocean Sediment Composition and Burial Flux in the Deep Sea. Global Biogeochem Cy 2021, 35 (4). https://doi.org/10.1029/2020gb006769.

(63) deRonde, C.; Massoth, G.; Baker, E.; Lupton, J. Volcanic, Geothermal, and Ore-Forming Fluids. 2005, 91–110. https://doi.org/10.5382/sp.10.06.

(64) Sonke, J. E.; Angot, H.; Zhang, Y.; Poulain, A.; Björn, E.; Schartup, A. Global Change Effects on Biogeochemical Mercury Cycling. *Ambio* **2023**, 1–24. https://doi.org/10.1007/s13280-023-01855-y.